

Tidal encounters of close white dwarf binaries with spinning black holesARYABRAT MAHAPATRA,¹ ADARSH PANDEY,¹ PRITAM BANERJEE,² AND TAPOBRATA SARKAR¹¹*Department of Physics, Indian Institute of Technology Kanpur, Kanpur 208016, India*²*Indian Institute of Astrophysics, Koramangala, Bangalore 560034, India***ABSTRACT**

When a stellar binary encounters a spinning black hole, interesting phenomena might result due to the mutual interaction between the binary spin, orbital angular momentum and the black hole spin. Here we consider such encounters between an intermediate mass spinning black hole and a close identical white dwarf binary system whose center of mass follows a parabolic trajectory. After studying a corresponding three-body problem in the point particle approximation, we perform a suite of smoothed particle hydrodynamics based numerical simulations of such scenarios. For this, we integrate the geodesic equations for the spinning black hole, while considering the hydrodynamics and the self and mutual gravitational interactions of the stars in a Newtonian approximation, an approach justified by the choice of parameters in the theory. We consider various initial configurations of the binary center of mass leading to equatorial and off-equatorial orbits, as also various initial inclinations between the binary's initial spin angular momentum and its initial orbital angular momentum. We find that the effects of black hole spin manifest clearly in the tidal dynamics of the binary components, while the observables of tidal encounters such as mass fallback rates are strongly dependent on the initial inclination angle. We show that the influence of the black hole spin emerges in distinct ways for different initial configurations of the binary's spin alignment. We establish that within the ambitions of the Hills mechanism, in certain cases, the fallback rate may show a three-hump structure, due to interactions between tidal debris of the individual stars.

1. INTRODUCTION

A binary stellar system that encounters a black hole is a classic example of a three body problem. Such problems have been studied for more than three centuries now, and a modern exposition can be found in the textbook of [Voltonen & Karttunen \(2005\)](#). The problem assumes importance in the context of astrophysical phenomena, as a significant number of stars are found in binary configurations ([Toonen et. al. 2017](#)). When a binary stellar system comes close enough to a black hole, tidal disruption events (TDEs) often result in observable signatures, that provides an ideal laboratory to test existing theories of gravitational interactions. In the context of three body problems involving a black hole and a stellar binary, point particle approximations for stars are easier to handle analytically and numerically, since one can integrate the geodesic equations under certain approximations of the self gravity between the two stars. However, the situation becomes more complicated when one considers stellar hydrodynamics as well. This is because stellar deformations and possible disruptions non-trivially affect the outcome of close encounters of binary stellar systems with black holes. Then, in the absence of enough symmetries, analytical computations are somewhat challenged. Numerical simulations are often employed to determine the nature of interaction in these cases, and a popular method is that of smoothed particle hydrodynamics (SPH).

In a recent previous paper ([Mahapatra et al. 2025](#)), we studied tidal encounters of close non-accreting white dwarf (WD) binaries with an intermediate mass black hole (IMBH) that was taken to be non-rotating. Here, we extend this analysis to rotating (Kerr) IMBHs. There are several motivations for the analysis performed in this paper. For example, most observed black holes are known to be spinning, with recent evidence suggesting that many of these can have spin parameters close to extremality. Thus studying the phenomenology associated with spinning BHs is important and

interesting in its own right, more so for IMBHs, whose observational evidence has been relatively rare compared to their super massive BH cousins. Stellar objects that have intrinsic spin are of further interest here, as their “coupling” with BH spin often results in rich physics, as was detailed in [Garain & Sarkar \(2024 b\)](#) for tidal encounters of spinning WDs with Kerr BHs. Binary star systems with large intrinsic angular momenta are expected to capture this feature to a greater extent. Also note that for spinning BHs which possess axial symmetry, off-equatorial orbits are important and interesting to study and a significant amount of literature exists on tidal interactions of solitary stars in such orbits. Stellar binaries assume importance in this context, since there exists larger freedom for the initial configuration of the system, which includes for example the relative interplay of the initial binary angular momentum about its centre of mass with the orbital angular momentum and the inclination of the orbit. All these put together makes the study of binary stellar systems in spinning black hole backgrounds important and interesting.

Here we present the results of a suite of SPH simulations that capture the effects of a spinning black hole background on a close WD binary. Our simulations integrate the Kerr BH geodesics along with a Newtonian treatment of the hydrodynamics of individual star, as well as the self gravity between them, as detailed in [Mahapatra et al. \(2025\)](#). To justify this approach, we note that the pericenter distance in our analysis is fixed at $25r_g$, with $r_g = GM/c^2$ being the gravitational radius, where Newtonian hydrodynamics remains a sufficiently robust approximation, see [Stone et. al. \(2019\)](#), [Tejeda et al. \(2017\)](#). Even at this “large” pericenter distance, the effects of the BH spin indicate richer physics compared to the non-spinning black hole, as we will argue in sequel. To the best of our knowledge, this scenario has not been studied in the literature, although studies on TDEs of solitary stars in equatorial and off-equatorial orbits in Kerr BH backgrounds are fairly abundant. For a sampling of the literature, see the works of [Rosswog, Ramirez-Ruiz & Hix \(2009\)](#); [Ramirez-Ruiz & Rosswog \(2009\)](#); [Beloborodov et al. \(1992\)](#); [Wiggins & Lai \(2000\)](#); [Ivanov, Chernyakova & Novikov \(2003\)](#); [Ishii, Shibata & Mino \(2005\)](#); [Ferrari, Gualtieri & Pannarale \(2009\)](#); [Kesden \(2012\)](#); [Singh & Kesden \(2024\)](#); [Haas et al. \(2012\)](#); [Hayasaki et al. \(2016\)](#); [Tejeda et al. \(2017\)](#); [Liptai et al. \(2019\)](#); [Banerjee et al. \(2019\)](#); [Gafton & Rosswog \(2019\)](#); [Janković & Gomboc \(2023\)](#). Further details and a more exhaustive set of references appear in [Mahapatra et al. \(2025\)](#).

2. METHODOLOGY AND INITIAL SETUP

In this section, we provide a brief description of the numerical methodology employed to simulate the tidal disruption of close WD binaries in a generic off-equatorial parabolic orbit around a spinning IMBH. [Banerjee et al. \(2023\)](#) presents all details on our SPH code to simulate the tidal disruption of a stellar fluid in the external gravitational field of a BH, that is inspired by the publicly available code PHANTOM ([Price et al. 2018](#)). To efficiently compute fluid properties and inter-particle forces, we employ a binary tree structure with an opening angle parameter set to $\theta_{\text{MAC}} = 0.5$. We adopt the standard SPH artificial-viscosity parameters $\alpha^{\text{AV}} = 1.0$ and $\beta^{\text{AV}} = 2.0$ ([Hayasaki et al. 2013](#)), along with the Balsara switch to suppress viscosity in shear flows ([Balsara 1995](#)). The SPH fluid equations are integrated using a leapfrog integrator (with global time-stepping), ensuring the exact conservation of energy and angular momentum throughout the simulation. To achieve a single stable WD configuration in SPH, we adopt the methodology outlined in [Garain et al. \(2023\)](#). We obtain the output density profile representing a carbon-oxygen WD in hydrostatic equilibrium from the stretch-mapping process ([Herant 1994](#)) in SPH. The final relaxed state of the WD used here satisfies the virial equilibrium condition, with deviations from viriality below 1%. Next, we introduce a close, detached circular binary of two identical low-mass WDs following the setup described in [Mahapatra et al. \(2025\)](#). Circular binaries are a reasonable initial choice, as close binaries in nature tend to circularize more rapidly than wide binaries, and ultimately settle into nearly circular orbits. Nevertheless, the eccentricity of the binary system can evolve significantly in the BH background, changing repeatedly as the system undergoes tidal separation during its interaction with the BH. We ensure that individual WDs experience no tidal deformations due to their companion, and that orbital oscillations remains free from dissipations or drift. The binary system is evolved for ≥ 15 orbital cycles, with deviations kept below 1%. Finally, the stable WD binary system is placed in the background of a rapidly spinning (Kerr) IMBH.

To investigate the tidal interactions with the centre of mass of the binary in a generic parabolic orbit, we adopt a hybrid formalism, in which we integrate the Kerr geodesics while implementing a Newtonian form of the fluid self-gravity, as we have mentioned before. The Kerr space-time in Boyer–Lindquist (BL) coordinates (t, r, θ, ϕ) is given by

$$ds^2 = - \left(1 - \frac{2GMr}{c^2\Sigma} \right) c^2 dt^2 - \frac{4GMra \sin^2 \theta}{c\Sigma} dt d\phi + \frac{\Sigma}{\Delta} dr^2 + \Sigma d\theta^2 + \left(r^2 + a^2 + \frac{2GMra^2 \sin^2 \theta}{c^2\Sigma} \right) \sin^2 \theta d\phi^2 \quad (1)$$

where $\Sigma = r^2 + a^2 \cos^2 \theta$ and $\Delta = r^2 - 2GMr/c^2 + a^2$, and c denotes the speed of light. The Kerr spin parameter is $a = J/(Mc)$, with M and J denoting the BH mass and angular momentum. The dimensionless spin parameter is

defined as $a^* = a/r_g$. To set the WD binary on an off-equatorial parabolic orbit, we must specify appropriate initial conditions: the initial coordinates and the initial velocity of the binary's centre of mass (CM), denoted (r_0, θ_0, ϕ_0) and $(\dot{r}_0, \dot{\theta}_0, \dot{\phi}_0)$, respectively. These are obtained by determining the turning points through the root finding approach of $dr/d\tau$, as done in Mahapatra et. al. (2024), following the procedure mentioned in Tejeda et al. (2017). For a parabolic trajectory, we require to solve the third-order polynomial equation

$$\mathcal{R}(r) = c^4 r_s r^3 - c^2 (l_z^2 + \mathcal{Q}) r^2 + l^2 r_s r - a^2 c^2 \mathcal{Q} , \quad (2)$$

where $r_s = 2r_g$, l^2 is the square of total magnitude of specific angular momentum and \mathcal{Q} is the Carter constant. The polynomial corresponds to the roots r_p , r_c and r_d . The pericentre distance r_p is evaluated from the definition of binary's impact parameter; $\beta^b = r_t^b/r_p$, where tidal radius of binary is given by:

$$r_t^b = R_{sep} \left(\frac{M}{M_b} \right)^{1/3} \quad (3)$$

Here, we consider $R_{sep} = a_0/2$, where, a_0 is the initial separation between the two stars in binary and M_b is the total mass of the binary system. The constants of motion can be written in terms of these roots as

$$\mathcal{Q} = \frac{c^2 r_s r_p r_c r_d}{a^2} , \quad l^2 = c^4 (r_p(r_c + r_d) + r_c r_d) , \quad l_z^2 = c^2 r_s \frac{a^2 (r_p + r_c + r_d) - r_p r_c r_d}{a^2} . \quad (4)$$

Additionally, we use the relation $l^2 = c^2 \mathcal{Q} + (l_z c - a \mathcal{E})^2$ and for a desired off-equatorial orbit with initial polar angle, $\theta_0 = \theta_a$ (to avoid any visual conflict with ϑ_0 introduced later), we have $d\theta/d\tau = 0 \implies \mathcal{Q} = l_z^2 \cot^2 \theta_a$. Once the roots are solved and the constants of motion are evaluated from Equation 4, then, substituting these into the first integrals of Kerr geodesics yield the initial velocity of the binary's CM.

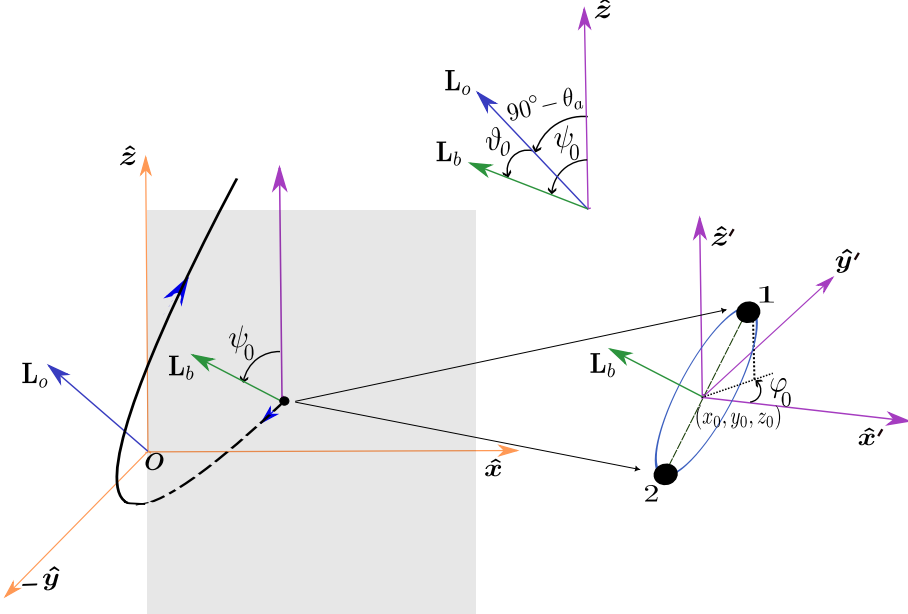


Figure 1. Qualitative depiction of binary stellar dynamics around a spinning BH.

A qualitative depiction of a generic binary system on a parabolic orbit around a spinning BH is given in Figure 1. The BH located at the origin O , with its spin either parallel or antiparallel to the z axis. The centre of mass of the binary is initialized at (x_0, y_0, z_0) , while its two components (which we take to be identical WDs) have their CMs at (x_{10}, y_{10}, z_{10}) and (x_{20}, y_{20}, z_{20}) , separated by a distance a_0 . The initial angular momentum of the binary about its centre of mass (\mathbf{L}_b) is oriented at an angle ϑ_0 relative to the initial orbital angular momentum (OAM) (\mathbf{L}_o) of the binary around the BH, computed about the origin. The binary phase angle, φ_0 denotes the initial angle made by

the line joining the binary components with the \hat{x} direction. By convention, angles are measured as positive in the directions indicated in the figure.

We choose the initial CM coordinates at a large distance from the BH, $r_0 = 10r_t^b \simeq 500r_g$. Further, to simplify the analysis, coordinates are chosen such that $\phi_0 = 0$ (so that the CM is initially on the x - z plane). The initial Cartesian position of the binary CM, $\mathbf{r}_{\text{CM}} = (x_0, y_0, z_0)$, is obtained via the standard transformation from spatial BL to Cartesian coordinates. The corresponding initial CM velocity, $\mathbf{v}_{\text{CM}} = (v_{x0}, v_{y0}, v_{z0})$, is computed by the similar transformation from the BL coordinate velocities $(\dot{r}_0, \dot{\theta}_0, \dot{\phi}_0)$.

According to our convention, a circular WD binary with initial separation a_0 , binary inclination ϑ_0 , and initial phase φ_0 (see Figure 1) is constructed by applying two successive Euclidean rotations. This procedure provides an excellent approximation at the large initial separations from the BH considered here, where spacetime curvature effects across the binary scale are negligible. Initially, we adopt a primed Cartesian coordinate system (x', y', z') that coincides with the global Cartesian axes (x, y, z) , and place the binary CM at the origin.

We begin by positioning the binary along the x' -axis. An anticlockwise rotation about the z' -axis by an angle φ_0 sets the initial orbital phase of the binary. This is followed by a clockwise rotation about the $+y'$ -axis by an angle ψ_0 , which imposes the desired binary inclination ϑ_0 . Finally, the binary CM is translated to its initial global position \mathbf{r}_{CM} , with the BH fixed at the origin of the coordinate system.

The initial Cartesian positions of the individual WD centers of mass, $\mathbf{x}_{i0} = (x_{i0}, y_{i0}, z_{i0})$, are then given by

$$\mathbf{x}_{i0} = \mathbf{r}_{\text{CM}} \pm \frac{a_0}{2} \left(\cos \psi_0 \cos \varphi_0, \sin \varphi_0, \sin \psi_0 \cos \varphi_0 \right), \quad (5)$$

where the plus (minus) sign corresponds to WD1 (WD2).

The corresponding initial velocities are

$$\mathbf{v}_{i0} = \mathbf{v}_{\text{CM}} \pm v_b \left(-\cos \psi_0 \sin \varphi_0, \cos \varphi_0, -\sin \psi_0 \sin \varphi_0 \right), \quad (6)$$

where $\psi_0 = (90^\circ - \theta_a + \vartheta_0)$, and $v_b = \sqrt{GM_{\text{WD}}/2a_0}$ denotes the characteristic orbital velocity of each WD within the binary.

The values for these initial conditions are finally determined by the tidal disruption parameters adopted in this study. We consider a tidal encounter between a rapidly spinning IMBH of mass $8 \times 10^3 M_{\odot}$ with spin parameter $a^* = \pm 0.98$ and an identical WD binary, where each WD has mass $M_{\text{WD}} = 0.5 M_{\odot}$, radius $R_{\text{WD}} = 0.0141 R_{\odot}$, and initial separation $a_0 = 6 R_{\text{WD}}$. To ensure that the interaction remains around a meaningful regime of our interest at $r_p \simeq 25 r_g$, we set $\beta^b = 2.0$, following from Equation 3.

Finally, we assign the remaining parameter values in order to explore how the tidal disruption dynamics depend on a^* , \mathbf{L}_b and \mathbf{L}_o . To this end, for our simulations, we consider either an off-equatorial orbit close to the meridional plane (defined by $\theta_a = 0^\circ$) with an initial value $\theta_a = 1^\circ$ or an equatorial orbit with an initial value $\theta_a = 90^\circ$. In the equatorial orbit, the binary has prograde motion around the BH when $a^* = +0.98$ and retrograde motion when $a^* = -0.98$. In these cases, we expect tidal effects to be maximal or minimal, as discussed in Mahapatra et. al. (2024). As there are a large number of parameters appearing in our formulation, we will simplify the analysis by fixing the initial phase, $\varphi_0 = 0^\circ$, and alter the inclination angle ϑ_0 . The essential physics of the phenomena that we study are captured in this choice, although the initial phase might play an significant role in determining some of the details, as pointed out in Mahapatra et al. (2025). In this work our intention is to understand the variation of the angle θ_a along with its offset ϑ_0 to exploit the axisymmetry of a Kerr black hole. We understand that the combinations of all three angles $(\theta_a, \vartheta_0, \varphi_0)$ is the ideal choice of study. However, due to its large parameter space we choose not to concentrate on the azimuthal offset phase in this paper. Rather, a culmination of all parameters is kept as a future work. We will make a few comments on the choice of the initial phase in the following Section 3.2 and in the concluding section of this paper.

Throughout this work, we adopt the convention that $\vartheta_0 = 0^\circ$ corresponds to prograde rotation of the binary spin relative to the OAM of the binary around the BH, while $\vartheta_0 = 180^\circ$ corresponds to retrograde rotation¹. This nomenclature will be used consistently in what follows. We also consider configurations with $\vartheta_0 = 90^\circ$, which represent cases where the binary spin lies on the orbital plane, directed towards the BH. For off-equatorial orbits, when the

¹ A retrograde configuration can be obtained either by reversing the initial binary spin or by rotating the binary by 180° ; the two are equivalent for an identical binary. In our simulations, we adopt the former approach, as both choices yield identical dynamics up to a relabelling of the stars. The same equivalence applies to any inclination ϑ_0 and its counterpart $\pi + \vartheta_0$.

binary spin is aligned with the $+z$ axis ($-z$ axis), the initial phase angle is set to $\psi_0 = 0^\circ$ ($\psi_0 = 180^\circ$). These choices correspond to binary inclinations

$$\vartheta_0 = \theta_a - 90^\circ \quad (\text{spin along } +z), \quad \vartheta_0 = \theta_a + 90^\circ \quad (\text{spin along } -z).$$

For an equatorial orbit ($\theta_a = 90^\circ$), these relations reduce to $\vartheta_0 = 0^\circ$ and $\vartheta_0 = 180^\circ$, respectively. In contrast, for an off-equatorial orbit with $\theta_a = 1^\circ$, they correspond to $\vartheta_0 = -89^\circ$ and $\vartheta_0 = 91^\circ$. Consequently, this makes our analysis restricted to configurations with three specific initial binary inclinations $\vartheta_0 = 0^\circ$, $\vartheta_0 \simeq 90^\circ$ and $\vartheta_0 = 180^\circ$.

3. POINT-PARTICLE DYNAMICS IN THE THREE-BODY PROBLEM

In this section, we describe the dynamics of the binary system by treating the stellar components as an initially bound pair of test particles orbiting a spinning BH. This simplified setup enables a comparative analysis for understanding how tidal interactions operate when the finite sizes of the stellar objects are later taken into account. Such finite-size effects can significantly modify the tidal dynamics through both the mutual gravitational influence of the companion and the hydrodynamics of each individual stellar component.

3.1. Tidal separation and binary spin effects

The evolution of a bound pair of particles constituting a circular binary and moving on a parabolic orbit around a spinning BH is governed by

$$\ddot{x}_a^i = - (g^{i\lambda} - g^{0\lambda} \dot{x}^i)_a \left[\left(\frac{\partial g_{\mu\lambda}}{\partial x^\nu} - \frac{1}{2} \frac{\partial g_{\mu\nu}}{\partial x^\lambda} \right) \dot{x}^\mu \dot{x}^\nu \right]_a - \frac{G m_b}{|x_a^i - x_b^i|^3} (x_a^i - x_b^i). \quad (7)$$

Here, the first term describes the motion of particles in the Kerr spacetime background and the second term accounts for the mutual self-gravity of the two particles. Using the solutions of Equation 7, we compute the individual particle trajectories for $a^* = \pm 0.98$ and $\theta_a = 1^\circ$, 90° . In the left panel of Figure 2, we show the trajectory for a binary whose initial binary spin has prograde rotation ($\vartheta_0 = 0^\circ$), while the corresponding retrograde case ($\vartheta_0 = 180^\circ$) is presented in the right panel.

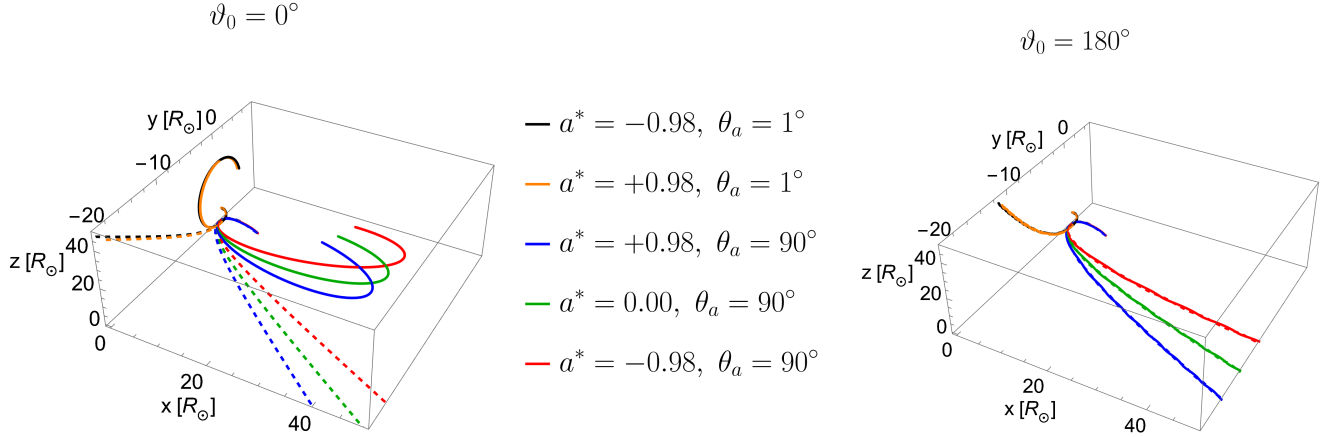


Figure 2. Trajectories of binary test particle around the spinning BH. **Left Panel:** The initial motion of the binary is prograde relative to the OAM ($\vartheta_0 = 0^\circ$). **Right Panel:** The initial motion of the binary is retrograde relative to the OAM ($\vartheta_0 = 180^\circ$).

We find that, for all combinations of parameters in the prograde rotation, the binary system undergoes tidal separation, one particle is captured onto a bound orbit around the BH, while the other is ejected onto a parabolic-like trajectory. This behaviour indicates the well-known Hills mechanism (Hills 1975). In contrast, for retrograde motion, the binary system preserves its bound state throughout the entire evolution, where the dynamics is not governed through Hills mechanism. For equatorial $\theta_a = 90^\circ$ orbits, the stronger apsidal precession produced for retrograde motion, drags the binary particle trajectories significantly closer to the BH compared to the prograde case. However, it is almost same in

$\theta_a = 1^\circ$ orbit for both $a^* = \pm 0.98$. Moreover, in both $\theta_a = 90^\circ$ and $\theta_a = 1^\circ$ configurations, the particle motion remains effectively confined to the orbital plane around the BH. Only a small deviation appears in the inner orbital motion of the binary for the $\theta_a = 1^\circ$ case. Note that by “inner orbital motion” we refer to the motion of the binary about its CM, whereas “outer orbital motion” indicates the motion of the binary around the BH.

If the initial binary inclination differs from the complete prograde or retrograde rotations, the motion is no longer expected to remain restricted to the orbital plane. As ϑ_0 increases from 0° toward 90° , we find that the tidal separation between the particle trajectories reduces following the Hills mechanism at pericentre, and the resulting bound elliptical orbits become progressively more compact. Figure 3 shows the trajectories for the case $\vartheta_0 = 90^\circ$, where the inner orbital motion of the binary is no longer aligned with its outer orbital motion. The resulting dynamics of the tidal encounter are qualitatively similar to those of the prograde rotation case. However, in $\vartheta_0 = 90^\circ$ case, the particle is caught into a smaller and more tightly bound elliptical orbit. For example, the outer orbit of particle 1 has a semi-major axis $a_1^{\text{out}} \simeq 2180 r_g$ (where $r_g = 0.017 R_\odot$) in the prograde rotation case, whereas it reduces to $a_1^{\text{out}} \simeq 1590 r_g$ for $\vartheta_0 = 90^\circ$. For higher initial binary inclinations ($\vartheta_0 > 90^\circ$), the Hills mechanism is progressively suppressed, and the tidal separation continues to decrease, allowing the binary to remain bound through pericentre passage. In these cases, the particles depart from the inner orbital motion at much later times, leading to highly eccentric bound orbits around the BH. Eventually, at $\vartheta_0 = 180^\circ$, the binary components never detach from their inner orbital motion, and the Hills mechanism ceases to operate entirely.

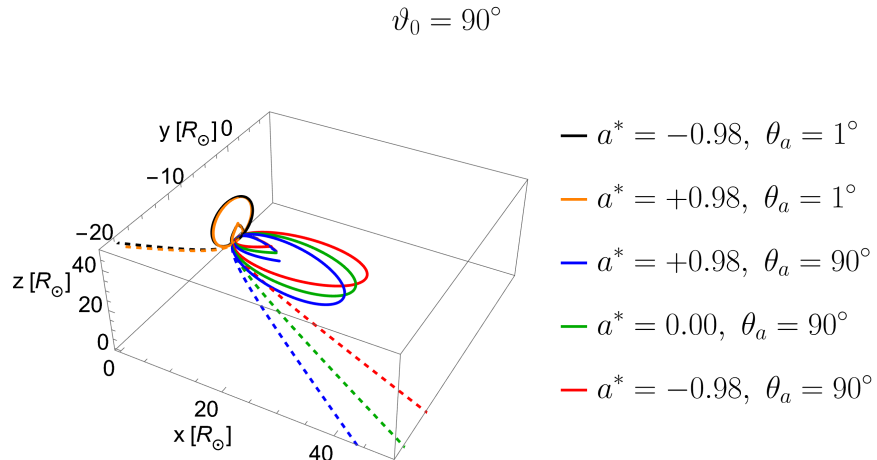


Figure 3. Trajectories of binary test particle around the spinning BH whose initial relative angular momenta of binary is subtended by $\vartheta_0 = 90^\circ$.

To understand these effects, we can examine how the binary spin is affected by the tidal torque exerted during the encounter with BH for different inclinations ϑ_0 . To this end, we compute the magnitude of the binary’s inner angular momentum (spin) for a range of initial inclinations, varying ϑ_0 from 0° to 180° for BH spin $a^* = -0.98$ and $\theta_a = 1^\circ, 90^\circ$ (a similar analysis can also be carried out for $a^* = 0.98$, but we omit this for brevity). In the left panel of Figure 4, we find that the magnitude of the binary spin diverges after pericentre passage for inclinations in the range $0^\circ \leq \vartheta_0 \lesssim 90^\circ$. For larger inclinations, $90^\circ < \vartheta_0 \leq 180^\circ$, the spin magnitude remains finite. This implies that the Hills mechanism operates most strongly for binaries whose initial inclinations lie between 0° and 90° . For larger inclination angles (particularly approaching towards retrograde rotation), the binary tends to retain its bound state more efficiently, and the tidal separation continues to decrease as the system transitions from prograde to retrograde configurations. We further find that the gain in the peak value of the binary spin magnitude is maximal for prograde configurations, decreases to a minimum near $\vartheta_0 = 90^\circ$, and then increases again toward the retrograde limit. This trend mirrors the behaviour of the binding energy of the particle captured during the Hills mechanism, suggesting a close correlation between the spin gain and the bound nature of the post-encounter orbit. Another important point is that the magnitude of the binary spin exhibits a significant difference between $\theta_a = 1^\circ$ and 90° cases for prograde rotation ($\vartheta_0 \simeq 0^\circ$). This difference gradually drops as ϑ_0 increases, and the spin magnitudes converge in the retrograde limit. Thus, the tidal torque acting on the binary leads to a significantly large gain in the spin magnitude for equatorial

encounters ($\theta_a = 90^\circ$) than for off-equatorial ones ($\theta_a = 1^\circ$) when the configuration is prograde rotation. In contrast, for retrograde configurations ($\vartheta_0 \simeq 180^\circ$), the gain is nearly same.

Now, to explore the remaining initial binary inclinations, we can consider configurations related by $\vartheta_0 \rightarrow -\vartheta_0$. For a non-spinning BH, these cases are redundant owing to the inherent symmetry in the relative alignment between the binary spin and its OAM. In this situation, we obtain identical outcomes for every pair ϑ_0 and $-\vartheta_0$, since both correspond to the same initial relative orientation of the binary spin with respect to the OAM. This symmetry also persists for equatorial orbits around a spinning BH, leading to identical outcomes (see the left panel of Figure 5), because the BH spin always remains aligned with the OAM. However, for off-equatorial orbits, the BH spin breaks this symmetry. As shown in the right panel of Figure 5, small but measurable differences arise for ϑ_0 and $-\vartheta_0$ due to the frame-dragging effects associated with the spinning BH in the $\theta_a = 1^\circ$ configuration. Consequently, our interest lies mainly within the range $0^\circ \leq \vartheta_0 \leq 180^\circ$ in this study.

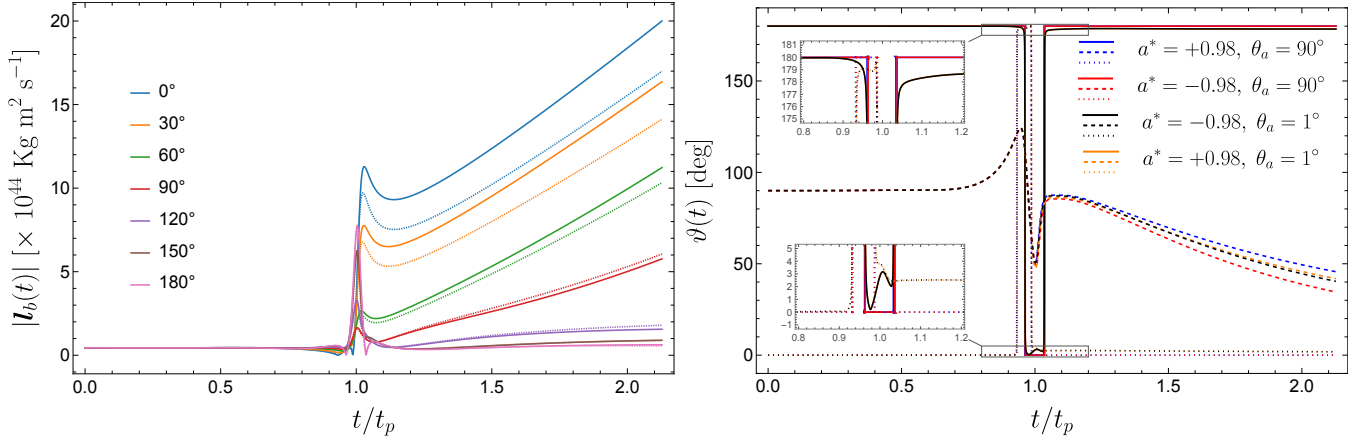


Figure 4. Evolution of the binary spin around a spinning BH. **Left Panel:** The change in magnitude of the binary spin, $|\mathbf{l}_b(t)|$ over normalized time (t/t_p , where $t_p = 0.0624$ hr is the pericentre time) for different initial binary inclinations ϑ_0 around spinning BH ($a^* = -0.98$). There is abrupt gain in the magnitudes of binary spin at t_p from its initial value, $|\mathbf{l}_b(0)| = |\mathbf{L}_b|$. The solid lines denote the values of $|\mathbf{l}_b(t)|$ in equatorial orbit, $\theta_a = 90^\circ$, and dashed lines denotes off-equatorial orbit, $\theta_a = 1^\circ$. **Right panel:** Reorientation of binary spin over time. $\vartheta(t)$ measures the orientation of \mathbf{l}_b with respect to \mathbf{L}_o . The dotted, dashed, and solid curves correspond to initial binary inclinations of $\vartheta_0 = 0^\circ$, 90° , and 180° , respectively.

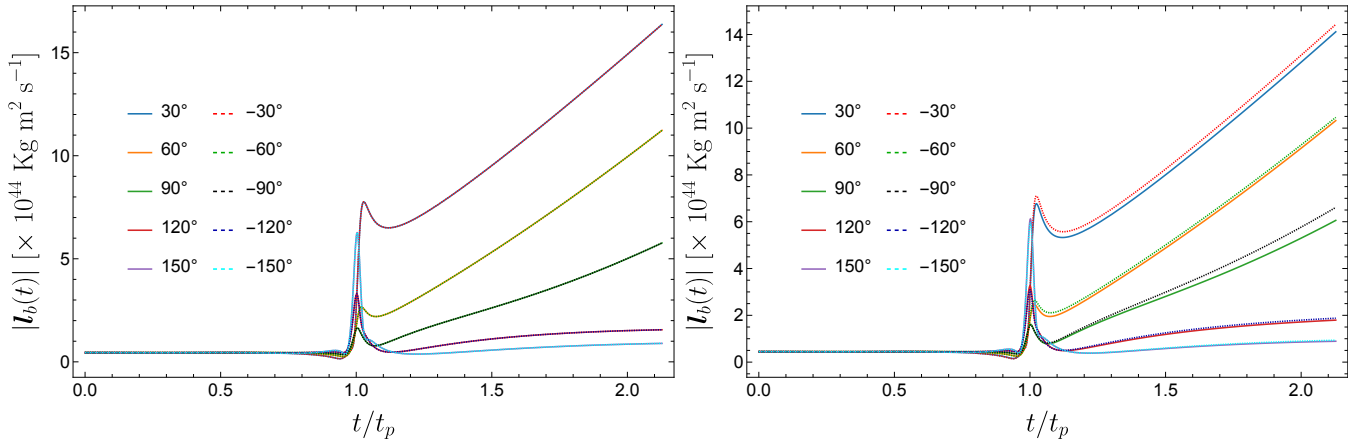


Figure 5. Evolution of the binary spin around a spinning BH ($a^* = -0.98$) for initial binary inclinations ϑ_0 and $-\vartheta_0$. **Left Panel:** Equatorial orbit ($\theta_a = 90^\circ$). **Right Panel:** Off-equatorial orbit ($\theta_a = 1^\circ$).

In these encounters, the tidal torque also alters the initial alignment of the binary's spin. We assess how the spin undergoes an abrupt reorientation near pericentre, including the influence of the BH spin. In the right panel of Figure 4, we show the evolution of the relative orientation of the binary spin, with respect to its initial OAM \mathbf{L}_o for three

inclinations ($\vartheta_0 = 0^\circ$, 90° , and 180°) and for different a^* and θ_a . We find that the binary experiences an almost complete orbital flip in both the prograde and retrograde rotations (denoted by solid and dotted lines respectively). Similar flipping effect of the binary spin has been analytically examined in earlier works by [Will \(2017\)](#), [Conway & Will \(2025\)](#), using higher-order multipole expansions of the Newtonian potential incorporating PN and relativistic corrections. However, in our case of spinning BH, where the dynamics follow the full Kerr geometry, we find that the orbital flip is less stable for the off-equatorial orbit than the equatorial one. For instance, as shown in the right panel of Figure 4, the black and yellow solid curves (identical for both $a^* = \pm 0.98$) barely reach 0° , and also they do not retain their initial alignment fully after pericentre passage. They exhibit a maximum relative deviation of $\sim 3^\circ$ compared to the equatorial case. Same can be seen for the prograde rotation(dotted lines). For $\vartheta_0 = 90^\circ$ case (dashed lines), the deviations from the initial spin orientation are maximum (after $t = t_p$) for the $a^* = -0.98$, $\theta_a = 90^\circ$ configuration than the other cases. These relative deviations can be attributed to the overall Lense–Thirring precession induced by the spinning BH in our setup. As is well known, around a spinning BH the Lense–Thirring effect induces nodal precession for off-equatorial orbits ([Lense & Thirring 1918](#); [Bardeen et al. 1972](#)). Consequently, when a rotating object orbits a spinning BH, it undergoes a wobbling motion. In our case, although the encounter occurs on a parabolic orbit, this single interaction is enough to introduce an overall instability in the orbital flip of binary spin corresponding to the off-equatorial orbit.

3.2. Dynamics due to the coupling effect of angular momenta

To investigate the coupling of binary spin with BH spin and/or with its OAM around the BH, we briefly account the resultant dynamics near pericentre. We compute the magnitude of the accelerations of each particle at pericentre time t_p for different values of θ_a , as shown in Figure 6. In the left panel, we compare the couplings: one in which the binary spin is aligned with its OAM ($\vartheta_0 = 0^\circ$), and another in which the binary spin is aligned with the z -axis ($\vartheta_0 = \theta_a - 90^\circ$). We find that the differences arise across different off-equatorial orbits, however, the differences for each individual particles do not grow by the same amount. Moreover, the accelerations in prograde rotations, increases for $a^* = -0.98$ as we go towards the equatorial orbit, while it decreases for $a^* = +0.98$ spin. This is unlike the behavior in $\vartheta_0 = -(90 - \theta_a)$ motion, where the acceleration either increases or decreases for both $a^* = \pm 0.98$. To highlight the relative strength of these couplings, we focus on the cases $\theta_a = 1^\circ$ and $\theta_a = 90^\circ$, where the differences are substantial for both $a^* = \pm 0.98$. Further, the outcomes in the coupling between the BH spin and the binary spin depends on whether the binary spin is aligned ($\vartheta_0 = \theta_a - 90^\circ$) or anti-aligned ($\vartheta_0 = 90^\circ + \theta_a$) with the z -axis. We therefore consider both possibilities and the resulting accelerations are compared (for $a^* = -0.98$) in the right panel. All these comparisons are meaningful only if we fix the binary phase to $\varphi_0 = 0^\circ$. Indeed, from a similar computation we found that most other values of φ_0 do not retain this relative differences in the strength of couplings. Therefore, the combination $\varphi_0 = 0^\circ$ with $\theta_a = 1^\circ$ and $\theta_a = 90^\circ$ constitutes a reasonable set of initial conditions that yields maximally distinguishable outcomes in our analysis. Accordingly, this combination is adopted as the representative setup for the analyses that follow.

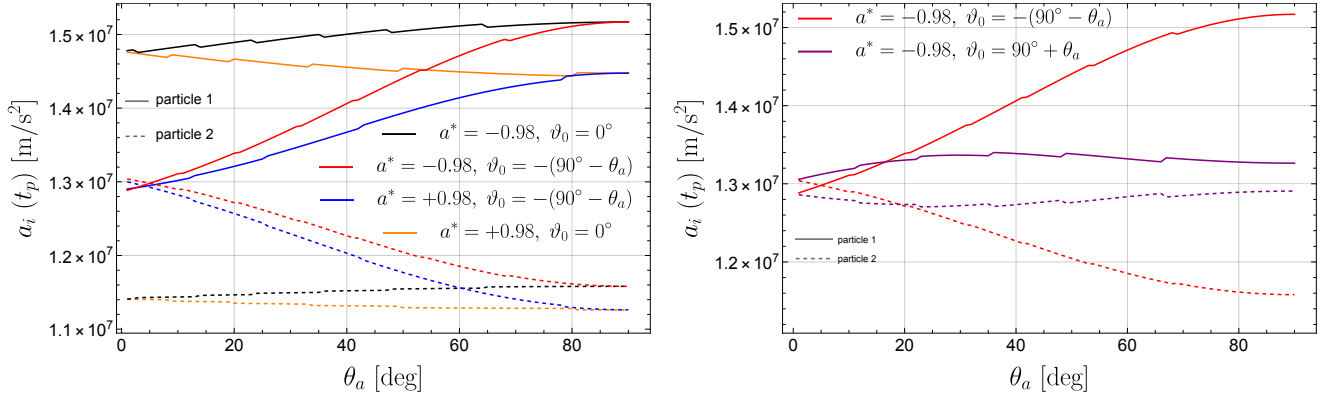


Figure 6. Comparison of acceleration magnitudes exerted on each individual particle between when binary spin - BH spin is coupled and binary spin - OAM is coupled.

4. DYNAMICS OF BINARY INCLUDING HYDRODYNAMICS AND FINITE STELLAR SIZES

Now we present the results of our numerical simulations. As mentioned before, we integrate the Kerr geodesic equations while the hydrodynamics and self gravity of the WDs are treated in a Newtonian approximation. We have run a suite of 15 SPH simulations in our study. The number of SPH particles is 3×10^5 particles per each WD. We have confirmed numerical convergence by running most of them with 10^5 particles per WD.

4.1. Mass disruption

The core mass fraction is calculated following the method described in [Mahapatra et al. \(2025\)](#). We first examine the case $a^* = 0$ and vary the binary inclination ϑ_0 ; the corresponding results are shown in left panel of Fig. 7. Throughout this analysis, we adopt an equatorial orbit². As the binary inclination is varied, the degree of tidal disruption experienced by WD1 and WD2 changes markedly. For inclinations up to $\vartheta_0 = 90^\circ$, one star is completely disrupted while the other undergoes only partial disruption. At $\vartheta_0 = 135^\circ$, both stars are fully disrupted. Once the orbital motion becomes retrograde, the roles of the two stars reverse: the star previously experiencing partial disruption is instead fully disrupted, consistent with expectations from the initial orbital geometry.

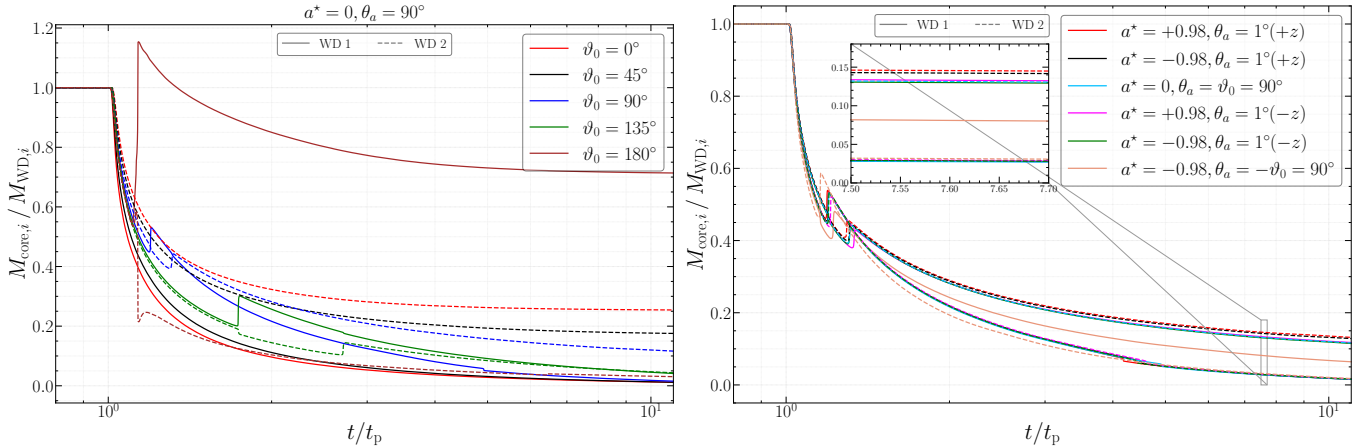


Figure 7. Bound core mass fraction, $M_{\text{core},i}/M_{\text{WD},i}$, for each WD as a function of t/t_p , where $i = 1, 2$ and $t_p \approx 0.062$ hr marks the time of pericenter passage. **Left panel:** Evolution for a non-spinning (Schwarzschild) BH for various initial binary inclinations ϑ_0 and phase $\varphi_0 = 0^\circ$. **Right panel:** Evolution in the presence of BH spin, with the initial binary spin either aligned or anti-aligned with the z -axis ($\vartheta_0 \approx \pm 90^\circ$) for the $\theta_a = 1^\circ$ orbit. For comparison, the cases $a^* = 0$, $\vartheta_0 = 90^\circ$ and $a^* = -0.98$, $\theta_a = -\vartheta_0 = 90^\circ$ are included, highlighting their similarity to the $\theta_a = 1^\circ$ and $\vartheta_0 \approx \pm 90^\circ$. An inset highlights regions where multiple cases overlap, forming three distinct bands: (i) red and black (dashed), (ii) magenta and green (solid) with deepskyblue (dashed), and (iii) the complementary set consisting of red and black (solid), magenta and green (dashed), and deepskyblue (solid).

A notable feature in the retrograde case is the pronounced interaction between the surviving stellar cores, which leads to mass exchange between them. Core–core mass transfer is also evident at $\vartheta_0 = 135^\circ$, where an increase in one core’s mass corresponds to a decrease in the other. In contrast, at $\vartheta_0 = 90^\circ$, the mass transfer proceeds from the tidal tail of one WD into the core of the other, as indicated by the rise of one core-mass curve without a corresponding decrease in the other. We also see here (as demonstrated in section 3.1) that the Hills mechanism indeed produces exchange-type interactions particularly for inclination angles up to $\vartheta_0 = 90^\circ$. Also, in $\vartheta_0 = 90^\circ$ case, we see inherent interactions develops among the disrupted materials of both WDs, despite the Hills mechanism driving the disrupted core to eject in a parabolic trajectory together with the disrupted tails, shown in Figure 14. This is because, the tidal separation between WDs in $\vartheta_0 = 90^\circ$ is quite less than the $\vartheta_0 = 0^\circ$ case (see left panel Figure 2 and Figure 3). For larger inclinations, the inherent interactions become more dominant due to the bound nature of binary, and the behaviour is primarily governed by the dynamics of the disrupted material of bound pair.

We next investigate the coupling between the binary spin and the BH spin, as well as the coupling between the binary spin and the OAM. For this purpose, we consider rapidly spinning BH with $a^* = +0.98$ and $a^* = -0.98$,

² In Schwarzschild spacetime, however, any orbital plane can be transformed into an equivalent equatorial configuration; therefore, the results are independent of the orbital plane.

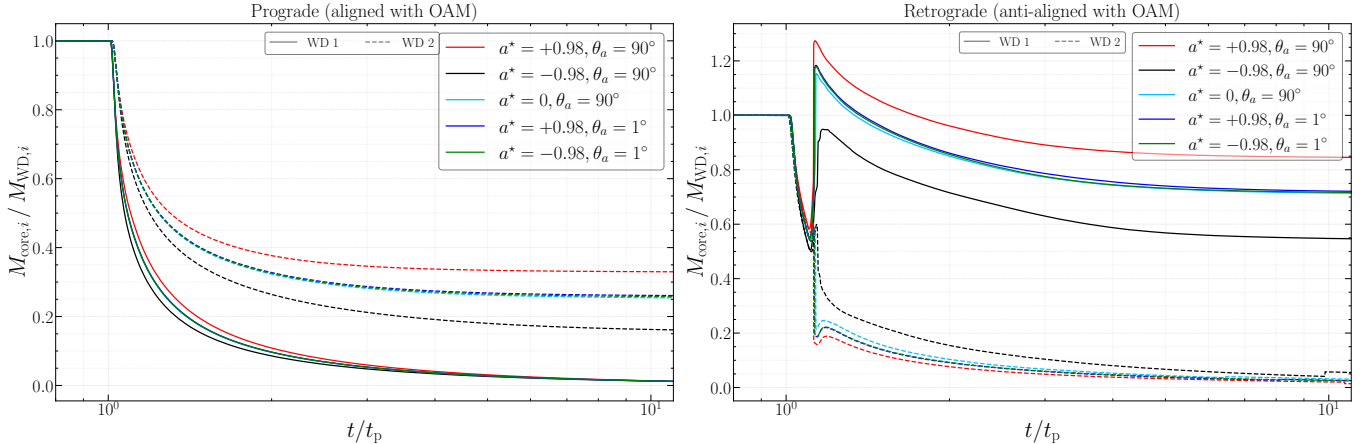


Figure 8. Bound core mass fraction, $M_{\text{core},i}/M_{\text{WD},i}$, for each white dwarf as a function of t/t_p , where $i = 1, 2$ and $t_p \approx 0.062$ hr denotes the time of pericenter passage. **Left panel:** Prograde binaries ($\vartheta_0 = 0^\circ$) orbiting a spinning BH, shown for both equatorial and off-equatorial orbits. **Right panel:** Retrograde binaries ($\vartheta_0 = 180^\circ$) orbiting a spinning BH, likewise shown for equatorial and off-equatorial orbits. For comparison, the corresponding $a^* = 0$ (non-spinning BH) prograde and retrograde cases are included in each panel.

for both equatorial and off-equatorial orbit, and for binary spins that are initially prograde or retrograde. The left panel of Figure 8 shows the prograde binary spin configurations. We find that the introduction of a positive BH spin ($a^* = +0.98$) reduces the disruption experienced by WD2 compared to the Schwarzschild case, while a negative BH spin ($a^* = -0.98$) enhances the disruption. For off-equatorial orbits with a small tilt ($\theta_a = 1^\circ$), the degree of disruption is similar to the $a^* = 0$ case for both signs of the BH spin, lying between the two equatorial-spin extremes.

These results qualitatively resembles the behavior observed in the case of a single spinning WD orbiting an spinning IMBH, as discussed extensively in Mahapatra et. al. (2024). In the retrograde binary-spin configurations (right panel of Figure 8), interaction between the stellar cores again leads to alternating increases and decreases in core mass. This time rather than disruption, we obtain the differences in the saturated mass of the WD1 by gaining material from its companion due to inherent interactions of the retrograde binary configuration. Nevertheless, the final saturated core mass of WD1 across different configurations follows the same qualitative trend observed for WD2 in the prograde case.

An especially interesting result arises in the right panel of Figure 7, which shows the core-mass evolution for orbits with $\theta_a = 1^\circ$ and binary spin lie along the $\pm z$ direction (which corresponds to almost a perpendicular type configuration in ϑ_0). In these configurations, the core masses closely track the $a^* = 0, \vartheta_0 = 90^\circ$ (binary spin lies in the orbital plane and points to the BH) Schwarzschild case. This behavior indicates that when the orbit is parallel to the BH spin (i.e., the OAM is perpendicular to the BH spin), the influence of BH spin is effectively suppressed, and the system behaves as if the BH were non-spinning. Among the spinning and non-spinning BH cases, the maximum disruption happens for $a^* = -0.98, \theta_a = -\vartheta_0 = 90^\circ$ (binary spin lies in the orbital plane and points away from the BH) case.

4.2. Tidal Stretching

To understand the relative tidal strength acting on each WD during the deformation that occurs near pericentre, we first analyze the evolution of the central density (expressed as ρ_{max}/ρ_0). Figure 9 shows the cases $\vartheta_0 = 0^\circ$ and $\vartheta_0 = 180^\circ$ in the left and right panels, respectively. For the $\vartheta_0 = 0^\circ$, WD 1 experiences rapid stretching compared to WD 2, ultimately leading to complete disruption. More importantly, the outcomes for different off-equatorial encounters are in proper correlation with the disruption behavior (see left panel of Figure 8). For $\vartheta_0 = 180^\circ$ case with $a^* = -0.98$, there is a small initial difference due to the varying off equatorial configurations, but later these maximum densities grow as the binary's inherent interactions dominate. Also, for $\vartheta_0 = 90^\circ$ or $\pi + 90^\circ$ (see left panel 10) case, the differences are small.

We can infer these relative tidal behavior in our configurations by measuring the eigenvalues of the tidal stress tensor at the regime we are working. It is also interesting to see how these eigenvalues behave across other far regimes than the conventional Newtonian outcome of (1, 1, -2). We evaluate the tidal stress tensor as, $C_{ij} = \frac{\partial f_i}{\partial x_j}$ at the pericentre, where the acceleration $f_i = g_{i\nu} \ddot{x}^\nu$ is obtained from Equations 1 and 7. In the right panel of Figure 10, we focus on the negative eigenvalue, the component responsible for stretching. At the pericentre $r_p \simeq 12.5 r_s$, this eigenvalue shows a clear

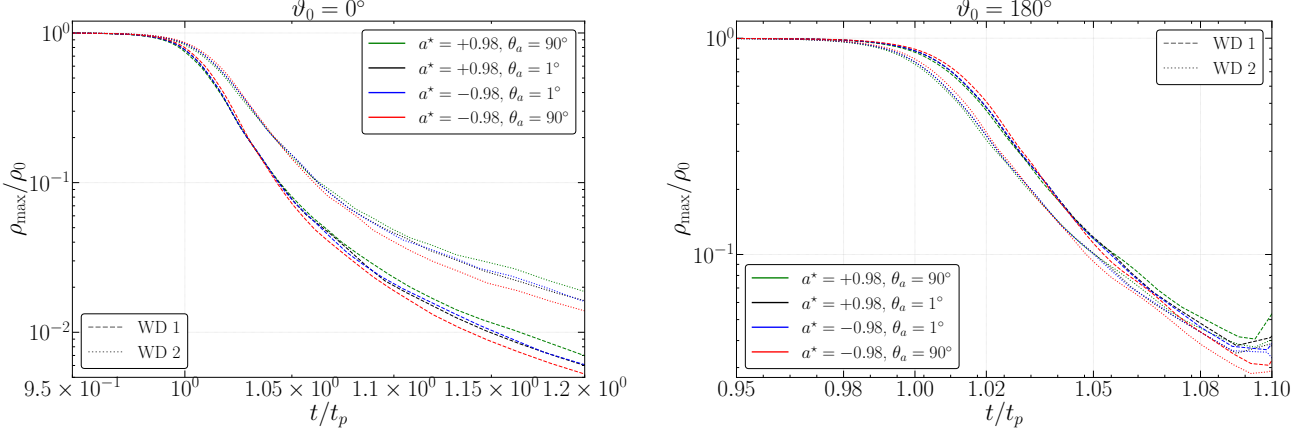


Figure 9. Evolution of the central density, ρ_{\max} (scaled by initial central density ρ_0) of WDs around the pericenter. **Left Panel:** Variation of ρ/ρ_{\max} over normalized time for initial inclination $\vartheta_0 = 0^\circ$. **Right Panel:** Variation of ρ/ρ_{\max} over normalized time for initial inclination $\vartheta_0 = 180^\circ$.

distinction between the two stars, with a small additional difference between the two orbital configurations, $\theta_a = 1^\circ, 90^\circ$. These differences gradually diminish and eventually diverge to large values beyond $\sim 30 r_s$. We verified that, in this regime, the binaries undergo extreme stretching as their separation decreases and they collide near pericentre. So, the divergence in the eigenvalue of the given star is caused by its companion rather than the BH, because the tidal force due to BH in this regime is already Newtonian in nature. The distinctions due to the different orbital configurations in $\vartheta_0 = 180^\circ$ case (see left panel of Figure 11) is found to be smaller than $\vartheta_0 = 0^\circ$ case, and their differences converge at higher r_p . In the right panel, the differences remain small due to varying orbital configurations and they fully converge around $50 r_s$.

Finally, from all the eigenvalues presented, we find that near pericentre the tidal strength exhibits more variations across different orbital configurations and between the companion WDs, particularly for the $\vartheta_0 = 0^\circ$ case. Therefore, differences in the mass-disruption outcomes emerge immediately after $t = t_p$ for this inclination. In contrast, for other inclination angles the differences become significant only after a time when the binary's inherent interactions begin to dominate, especially in the $\vartheta_0 = 180^\circ$ configuration.

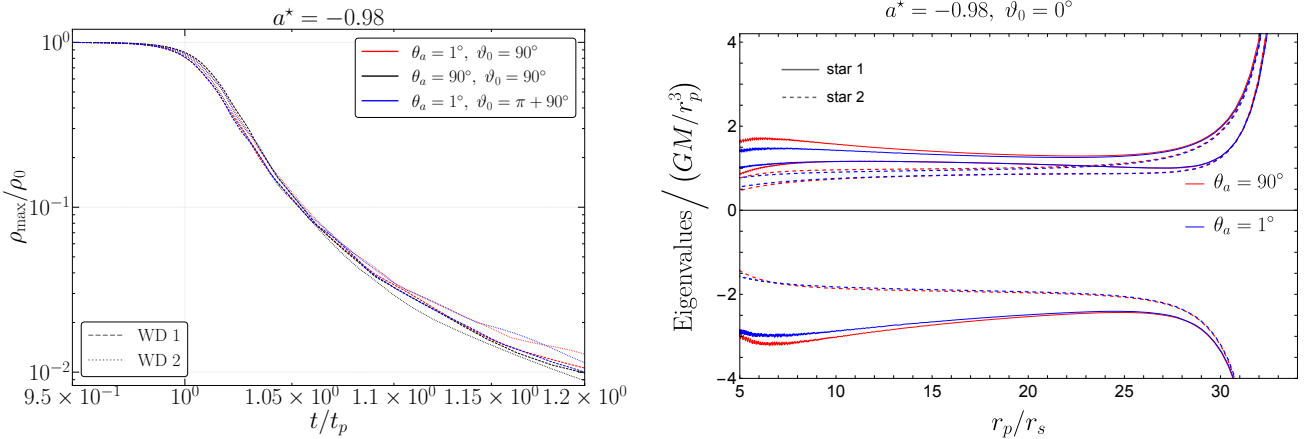


Figure 10. **Left Panel:** Variation of ρ/ρ_{\max} over normalized time for initial inclination around BH spin ($a^* = -0.98$) in $\theta_a = 1^\circ$ orbit (perpendicular with OAM). In $\theta_a = 90^\circ$, binary spin, OAM and BH spin, all are perpendicular to each other. **Right Panel:** Eigenvalues of C_{ij} vs pericentre distance (scaled by Schwarzschild radius r_s) for initial inclination $\vartheta_0 = 0^\circ$ around BH with $a^* = -0.98$.

4.3. Fallback rates

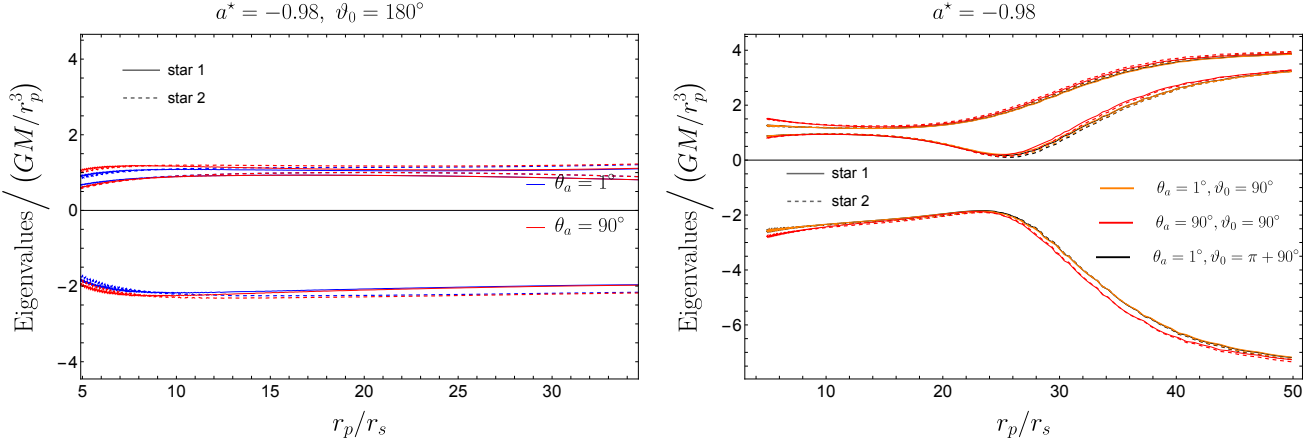


Figure 11. Eigenvalues of C_{ij} vs pericentre distance (scaled by Schwarzschild radius r_s) around BH with spin $a^* = -0.98$. **Left Panel:** For initial inclination $\vartheta_0 = 180^\circ$. **Right Panel:** Initial inclinations are set such that they are almost along BH spin ($\pm \hat{z}$) and perpendicular with OAM.

The left panel of Figure 12 shows the fallback rates for the non-spinning black hole case ($a^* = 0, \theta_a = 90^\circ$) for different binary inclinations ϑ_0 , with the initial binary phase fixed at $\varphi_0 = 0$. We find that the late-time fallback does not always follow the canonical $t^{-5/3}$ power-law decay. In particular, the $\vartheta_0 = 180^\circ$ configuration exhibits a more complex evolution: at intermediate times the fallback rate decays more slowly, approximately as $t^{-7/5}$, before transitioning at later times to a steeper decline, close to $t^{-9/4}$. In contrast, all other inclination angles adhere closely to the standard $t^{-5/3}$ behaviour over the late-time regime. Further, as we predicted the nature of bound trajectories in section 3, accordingly we observe that the peak fallback time, t_{peak} is obtained earlier when the disruption takes place in a more tightly bound orbit determined by the corresponding ϑ_0 . This diversity in fallback behaviour is notable and underscores the strong sensitivity of the fallback dynamics to the initial orientation of the binary.

For the Schwarzschild case only, we compute the fallback rate using the frozen-in energy approximation. In all subsequent figures, the fallback rates are obtained by numerically differentiating the mass accumulated within a radius of $3r_t$ as a function of time; nevertheless, the Schwarzschild result is retained in each panel for comparison. This provides a useful baseline against which the late-time behaviour of the spinning BH cases can be predicted.

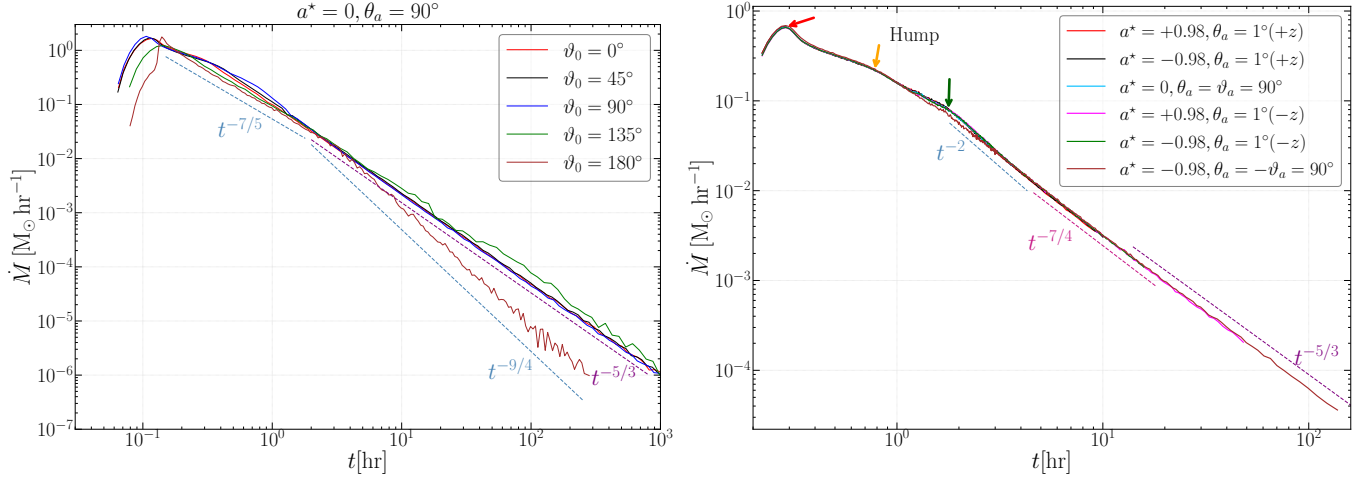


Figure 12. Fallback rate, \dot{M} , as a function of time (in hours). **Left panel:** Results for a non-spinning (Schwarzschild) BH for various initial binary inclinations ϑ_0 and phase $\varphi_0 = 0^\circ$. **Right panel:** Results for a spinning BH, with the initial binary spin aligned or anti-aligned with the z -axis ($\vartheta_0 \approx \pm 90^\circ$) for the $\theta_a = 1^\circ$ orbit. For comparison, the cases $a^* = 0, \vartheta_0 = 90^\circ$ and $a^* = -0.98, \theta_a = -\vartheta_0 = 90^\circ$ are included, highlighting their similarity to the $\theta_a = 1^\circ$ and $\vartheta_0 \approx \pm 90^\circ$. The arrows highlight the *three-hump structure*, with the colours corresponding to different ranges of bound specific energy as discussed in the subsequent section.

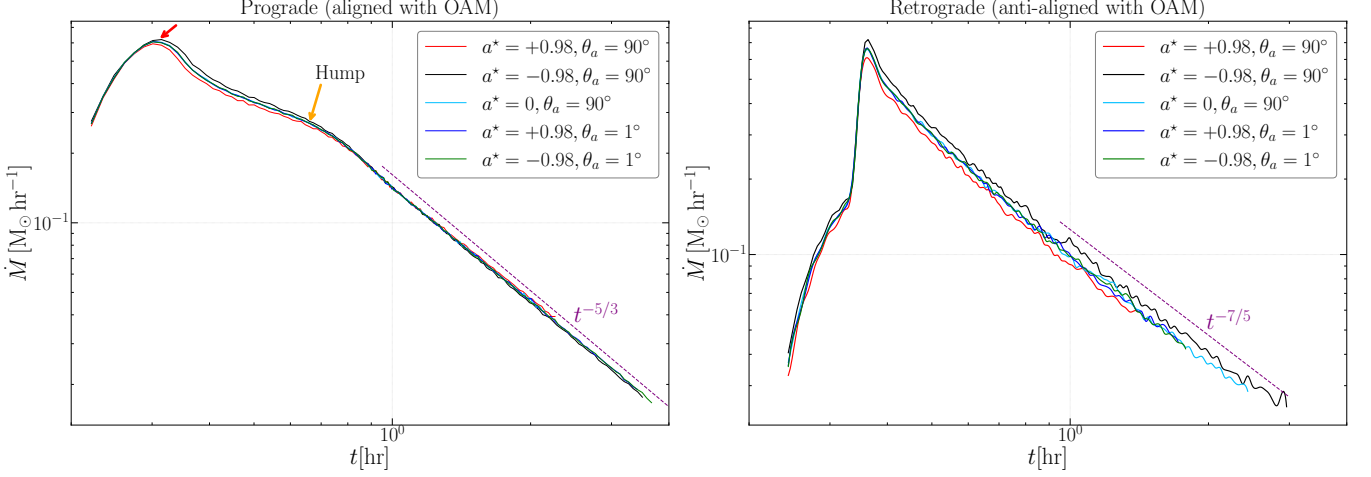


Figure 13. Fallback rate, \dot{M} , as a function of time (in hours). **Left panel:** Prograde binaries ($\vartheta_0 = 0^\circ$) orbiting a spinning BH, shown for both equatorial and off-equatorial orbits. The arrows highlight the double hump feature visible in the prograde case, with the colours corresponding to different ranges of bound specific energy as discussed in the subsequent section. **Right panel:** Retrograde binaries ($\vartheta_0 = 180^\circ$) orbiting a spinning BH, likewise shown for equatorial and off-equatorial orbits. For comparison, the corresponding $a^* = 0$ (non-spinning BH) prograde and retrograde cases are included in each panel.

Introducing BH spin leads to distinct and systematic changes in the fallback behaviour. For prograde binaries (see left panel of Figure 13), both in the equatorial and off-equatorial configurations, the fallback curves conform remarkably well to the $t^{-5/3}$ scaling across all inclinations. By contrast, retrograde binaries (see right panel of Figure 13) deviate from this trend, displaying a shallower late-time decay approaching $t^{-7/5}$. The influence of BH spin in $\theta_a = 90^\circ$ is also clearly reflected in the peak fallback rates, which follow the hierarchy

$$\dot{M}_{\text{peak}}(a^* = -0.98) > \dot{M}_{\text{peak}}(a^* = 0) > \dot{M}_{\text{peak}}(a^* = +0.98).$$

For retrograde encounters, the spin-induced differences persist even at late times: the $a^* = -0.98$ case maintains the highest fallback rate among the three. This behaviour arises because the stronger apsidal precession associated with retrograde orbits brings the returning debris closer to the BH, enhancing the mass return rate.

An interesting behaviour emerges for binaries whose spin is aligned along $\pm z$ in $\theta_a = 1^\circ$, as well as for systems with binary inclination $\vartheta_0 = 90^\circ$ in the equatorial plane (see right panel of Figure 12). In these configurations, the fallback curves display a distinct *three-hump structure*, highlighted by arrows in the figure, that is different from the conventional two-hump pattern characteristic of typical binary disruptions. The late-time decay initially steepens to a slope close to t^{-2} , before transitioning to a shallower behaviour of approximately $t^{-7/4}$. At even later times, the fallback rate approaches the canonical $t^{-5/3}$ scaling. Comparison with the corresponding Schwarzschild case also indicates that, at sufficiently late times, the fallback rate asymptotically recovers the standard $t^{-5/3}$ behaviour. This sequence of evolving power-law indices reflects a transient phase in which the debris dynamics are strongly influenced by relativistic effects and interactions, rather than a permanent departure from the standard fallback behaviour.

Note that stronger precession can drive debris closer to the black hole on subsequent passages, steepening the fallback rate at intermediate times, while the gradual phase mixing of the debris ultimately restores the decay expected from the frozen-in energy distribution. Taken together, these results point to a richer and more intricate interplay between orbital geometry, internal binary orientation, and relativistic precession in tidal disruption events than previously appreciated.

4.3.1. A brief note on the three-hump structure

In Figure 14, we present the snapshots from two late-time stages of the post-disruption simulation for the $a^* = 0$ and $\vartheta_0 = 90^\circ$ case. In the left panel, the inner bound tails accrete onto the BH, where the debris is shown in red, orange, and green, each corresponding to a distinct range of negative specific energies. These contribute sequentially to the hump-like features seen in the fallback curve (see the right panel of Figure 12). In contrast, for the $\vartheta_0 = 0^\circ$ configuration, Figure 15 shows that only the bound debris (shown in red and orange) contributes to the two-hump structure of the fallback curve (see the left panel of Figure 13).

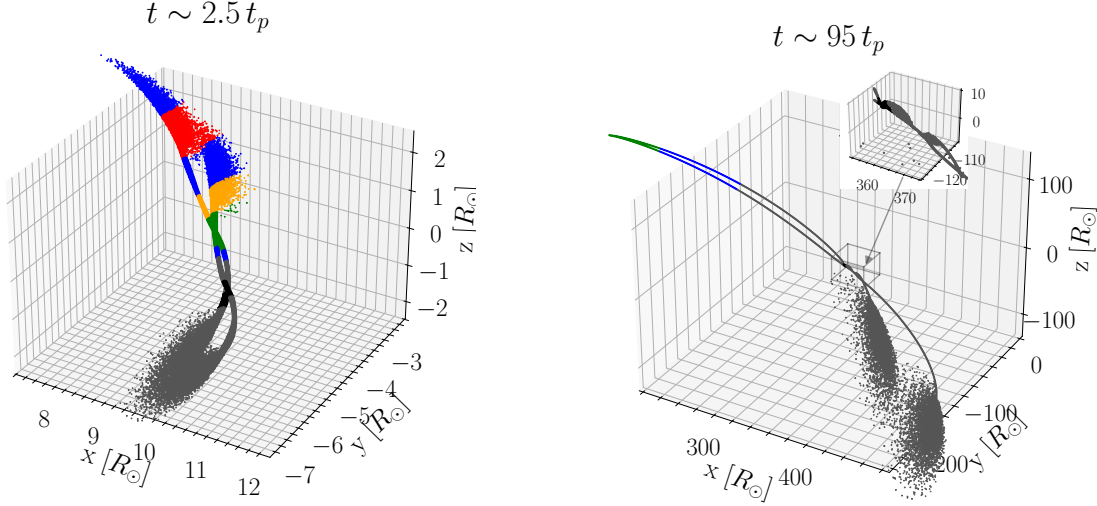


Figure 14. Close-range snapshots from post-disruption simulations of a tidal encounter at inclination $\vartheta_0 = 90^\circ$ for $a^* = 0$ case. The disrupted material is shown using a colour-coded distribution, where each colour corresponds to debris of specific energies. Red, orange, green, and blue denote debris with negative specific energies, each contributing to a specific part of the fallback curve. While black marks the core particles and the rest of the material shown in grey has positive specific energy. **Left panel:** Snapshot taken at $t \sim 2.5 t_p$, prior to the peak fallback rate \dot{M}_{peak} . The tidal streams from both disrupted WDs wind around each other. The inner bound tails are accreting onto the BH, while the cores of both WDs are drawn together and undergo disruption. The unbound outer tails hangs behind the cores. **Right panel:** Snapshot taken at $t \sim 95 t_p$, where the late time behavior of fallback curve is guided by the remaining accreting debris (denoted by green and blue). The ejected WD has undergone partial disruption and its remnant core saturates at a lower mass. It holds the two outer tidal streams of both disrupted WDs, which are tied up together. An inset highlights this region with a clearer view.

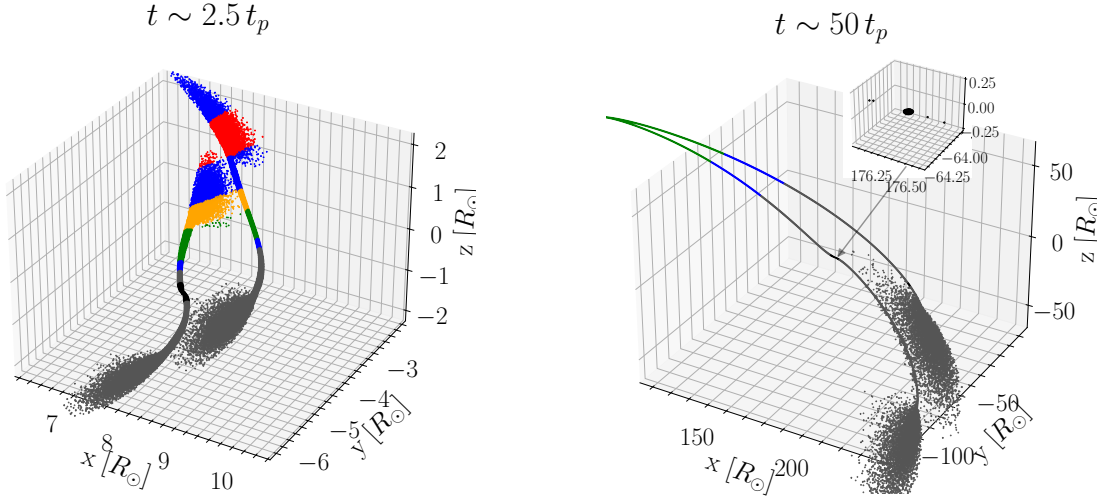


Figure 15. Close-range snapshots from post-disruption simulations of a tidal encounter at inclination $\vartheta_0 = 0^\circ$ for $a^* = 0$ case. **Left panel:** Snapshot taken at $t \sim 2.5 t_p$, prior to the peak fallback rate \dot{M}_{peak} . The tidal streams from both disrupted WDs remains apart from each other. **Right panel:** Snapshot taken at $t \sim 50 t_p$. The ejected WD has undergone partial disruption and its remnant core saturates at a lower mass. An inset highlights this region with a clearer view.

We can comparatively estimate the overall distribution of the disrupted material by examining the total debris differential mass distribution, $dM/d\epsilon$ with respect to specific energy in Figure 16. This distribution is quantified using the characteristic energy spread of the debris, $\Delta\epsilon = GMR_{\text{bin}}/(r_t^b)^2$, where $R_{\text{bin}} = R_{\text{sep}} + R_{\text{WD}}$. We find that the inner

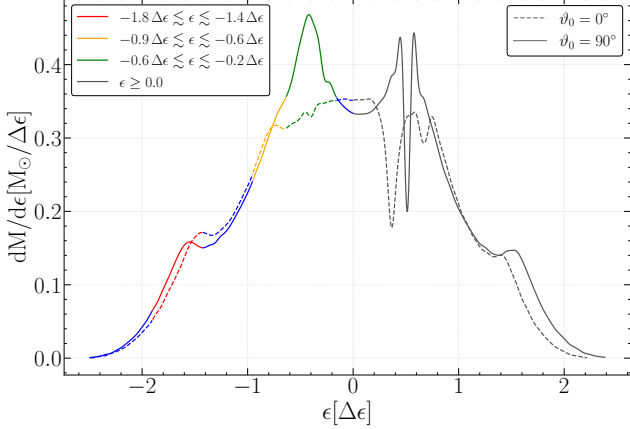


Figure 16. The variation in the total debris differential mass distribution, $dM/d\epsilon$ with respect to the specific energy ϵ for $a^* = 0$ case. The solid and dashed lines denotes $\vartheta_0 = 0^\circ$ and $\vartheta_0 = 90^\circ$ configurations respectively. The coloured regions correspond to the indicated ranges of specific energies spanned by the debris. The remaining bound material outside these energy ranges is shown in blue.

tail of WD1 containing a large fraction of the debris (shown in red), gives rise to the first hump in the fallback curve. Subsequently, the inner tail of WD2 together with a portion of the neck region of WD1 (collectively shown in orange) contributes the second hump. Now, in the $\vartheta_0 = 90^\circ$ configuration, the third hump is produced by the merged region of the two tidal streams (shown in green), where maximum amount of debris are clustered around the same specific bound energy. This clustering of matter can enhance the role of self-gravity within that region, drawing additional material toward it and leading to more mass clumped within a narrow of range of specific energies, as seen in Figure 16. However, this is absent in $\vartheta_0 = 0^\circ$ configuration, where the debris in the same specific energy range (shown in green) from the two tidal streams remains separated from each other. As a result, the debris distribution in this range is nearly flat (see Figure 16), producing neither an additional hump nor a change in slope in the resulting fallback curve.

The remaining bound debris (shown in blue) contributes to the other portions of the fallback curve. Black marks the core particles and rest of the material shown in grey also do not contribute to the fallback curve, instead escape on a parabolic trajectory later.

5. DISCUSSIONS AND CONCLUSIONS

In this paper, we have undertaken a comprehensive analysis of tidal interactions of a close WD binary with an IMBH. Apart from the intrinsic interest in IMBHs for which observational literature is relatively less compared to their super-massive BH cousins, our results in this paper offer new insights into the rich physics of the dynamics of a WD binary in such BH backgrounds and highlights the intricate interplay between the BH spin, binary spin and binary OAM. We have considered cases when the CM of the binary is initially in the equatorial plane or close to the meridional plane, with an initial inclination between the binary OAM and spin to be $0^\circ, 90^\circ$ and 180° . These reasonably cover the possible range of the initial binary configuration, with maximally distinguishable results.

In particular, our results indicate that while BH spin non-trivially influences the outcome of the TDEs in terms of the core mass, the binary inclination plays a central role in deciding the observables, for example the fallback rate of debris into the BH. In the previous work Mahapatra et al. (2025), we demonstrated how observable outcomes depend on the initial binary phase φ_0 . From the fallback-rate calculations, we found that for prograde configurations the fallback curves were largely identical, whereas in retrograde configurations the detailed structure, such as the presence of humps, the late-time slope, and the peak fallback rate \dot{M}_{peak} varied significantly. This holds in a qualitatively similar way in the present study for $\vartheta_0 = 0^\circ$ and $\vartheta_0 = 180^\circ$. This happens because, for $\vartheta_0 = 180^\circ$, the binary tends to remain bound, leading to strong internal interactions between the disrupted companions, which in turn modify the fallback curve. In contrast, for $\vartheta_0 = 0^\circ$, the binary undergoes a clean Hills-type tidal separation, and the disrupted components do not interact, resulting in a similar fallback behaviour for both sets of debris.

Similarly, for the $\vartheta_0 = 90^\circ$ configuration, we have checked from a few simulations where the tidal encounter again proceeds via a Hills-type mechanism even for different values of φ_0 . As a result, the interactions between the disrupted components are relatively less (in some cases none), and the partially disrupted core is ejected along with the outer

tidal tails. Consequently, the overall nature of the fallback curve is not strongly affected by variations in φ_0 . We further emphasize that the differences in tidal outcomes across orbital configurations (characterized by a^* and θ_a) and between the two WDs are maximum for the $\vartheta_0 = 0^\circ$ case. For other binary inclination angles, these differences become significant only after interactions between the disrupted companions begin to dominate, particularly in the $\vartheta_0 = 180^\circ$ configuration. Finally, we mention that the three-hump behaviour in the fallback rate that we have seen here is an artefact of binary spin and this feature will also present in non-spinning black hole backgrounds.

Acknowledgements

We acknowledge the support and resources provided by PARAM Sangam under the National Supercomputing Mission, Government of India, at the Indian Institute of Technology Kanpur. The work of AM is supported by Prime Minister's Research Fellowship by the Ministry of Education, Govt. of India.

Data Availability Statement

The data underlying this article will be shared upon reasonable request to the corresponding author.

REFERENCES

Balsara, D. S. 1995, Journal of Computational Physics, 121, 357. doi:10.1016/S0021-9991(95)90221-X

Banerjee, P., Paul, S., Shaikh, R., & Sarkar, T. 2019, Phys. Lett. B, 795, 29. doi:10.1016/j.physletb.2019.05.048

Banerjee, P., Garain, D., Chowdhury, S., et al. 2023, MNRAS, 522, 4332. doi:10.1093/mnras/stad1284

Bardeen, J. M., Press, W. H., & Teukolsky, S. A. 1972, ApJ, 178, 347. doi:10.1086/151796

Beloborodov, A. M., Illarionov, A. F., Ivanov, P. B., & Polnarev, A. G. 1992, MNRAS, 259, 209. doi:10.1093/mnras/259.2.209

Conway, L. & Will, C. M. 2025, PhRvD, 111, 8, 083052. doi:10.1103/PhysRevD.111.083052

Ferrari, V., Gualtieri, L., & Pannarale, F. 2009, CQGra, 26, 125004. doi:10.1088/0264-9381/26/12/125004

Gafton, E., & Rosswog, S. 2019, MNRAS, 487, 4790. doi:10.1093/mnras/stz1530

Garain, D., & Sarkar, T., 2024 ArXiv: 2401.17031 [astro-ph.HE]

Garain, D., Banerjee, P., Chowdhury, S., et al. 2023, arXiv:2307.03142. doi:10.48550/arXiv.2307.03142

Haas, R., Shcherbakov, R. V., Bode, T., & Laguna, P. 2012, ApJ, 749, 117. doi:10.1088/0004-637X/749/2/117

Hayasaki, K., Stone, N., & Loeb, A. 2013, MNRAS, 434, 909. doi:10.1093/mnras/stt871

Hayasaki, K., Stone, N., & Loeb, A. 2016, MNRAS, 461, 3760. doi:10.1093/mnras/stw1387

Herant, M. 1994, Mem. Soc. Astron. Italiana, 65, 1013.

Hills, J. G. 1975, Nature, 254, 295. doi:10.1038/254295a0

Ishii, M., Shibata, M., & Mino, Y. 2005, Phys. Rev. D, 71, 044017. doi:10.1103/PhysRevD.71.044017

Ivanov, P. B., Chernyakova, M. A., & Novikov, I. D. 2003, MNRAS, 338, 147. doi:10.1046/j.1365-8711.2003.06028.x

Janković, T., & Gomboč, A. 2023, ApJ, 946, 25. doi:10.3847/1538-4357/acb8b0

Kesden, M. 2012, Phys. Rev. D, 86, 064026. doi:10.1103/PhysRevD.86.064026

Lense, J. & Thirring, H. 1918, Physikalische Zeitschrift, 19, 156.

Liptai, D., Price, D. J., Mandel, I., et al. 2019, arXiv:1910.10154. doi:10.48550/arXiv.1910.10154

Mahapatra, A., Pandey, A., Garain, D. et. al. 2024 ArXiv: 2410.12727 [gr-qc]

Mahapatra, A., Pandey, A., Banerjee, P., et al. 2025, , arXiv:2508.03463. doi:10.48550/arXiv.2508.03463

Price, D. J., Wurster, J., Tricco, T. S., et al. 2018, PASA, 35, e031. doi:10.1017/pasa.2018.25

Rosswog, S., Ramirez-Ruiz, E., & Hix, W. R. 2009, ApJ, 695, 404. doi:10.1088/0004-637X/695/1/404

Ramirez-Ruiz, E., & Rosswog, S. 2009, ApJ, 697, L77. doi:10.1088/0004-637X/697/2/L77

Singh, T., & Kesden, M. 2024, Phys. Rev. D, 109, 043016. doi:10.1103/PhysRevD.109.043016

Stone, N. C., Kesden, M., Cheng, R. M., et al. 2019, General Relativity and Gravitation, 51, 30. doi:10.1007/s10714-019-2510-9

Tejeda, E., Gafton, E., Rosswog, S., et al. 2017, MNRAS, 469, 4, 4483. doi:10.1093/mnras/stx1089

Toonen, S., M., Hollands, M., Gansicke, B. T., et al. 2017 A&A, 602, A16. doi:10.1051/0004-6361/201629978

Voltonen, M., & Karttunen, H., *The three body problem* Cambridge University Press, 2005.

Wiggins, P., & Lai, D. 2000, *ApJ*, 532, 530.
doi:10.1086/308565

Will, C. M. 2017, *PhRvD*, 96, 023017,
doi:10.1103/PhysRevD.96.023017